A Physics-Based Approach to Trim Optimization of Coaxial Helicopters in High-Speed Flight

George Jacobellis
Graduate Research Assistant
Rensselaer Polytechnic Institute
Troy, New York, USA

Farhan Gandhi
Professor
Rensselaer Polytechnic Institute
Troy, New York, USA

Matthew Floros
Research Engineer
U.S. Army Research Laboratory
Aberdeen Proving Ground, MD, USA

ABSTRACT

Optimal trim was investigated for a lift-offset coaxial helicopter in high speed flight. An RCAS model of the XH-59 Advancing Blade Concept demonstrator aircraft was developed for the study and flight test trim conditions at 250 kts were used for baseline trim. The effects of varying redundant controls including rotor speed, auxiliary thrust, and differential lateral pitch were examined by trimming the aircraft at a variety of different trim states. Low power and low vibration trim states were identified and the performance and vibratory loads of these trim points were compared to the baseline trim condition. Reduction in power requirements of 17% were observed for a reduction in rotor speed combined with reduced differential lateral pitch. Power savings came in part from rotor slowing and the corresponding re-distributing of rotor lift and avoiding drag divergence at the advancing blade tips. The optimized trim state also resulted in an aft tilt of the tip path plane and upwash through the rotor disk, further decreasing main rotor power. Decreasing the blade pitch on the retreating side through a reduction in differential lateral pitch resulted in reduction of reverse flow drag. Rotor slowing was limited to 70% of the nominal RPM because of resonance of the rotor first flap and chordwise modes at the 2/rev frequency. Further reductions in rotor speed produced a small reduction in power required but large increases in vibratory loads.

NOMENCLATURE

(x,y,z)	Vehicle coordinate system, oriented positive (aft, starboard, up)
A	Longitudinal trim variable
B	Lateral trim variable
D	Drag
F	Rotor force
H	Rotor longitudinal force, positive aft
LOS	Lift-offset (%)
M	Rotor moment
P	Power
R	Rotor radius
T	Rotor thrust
V_∞	Freestream velocity
ψ	Rotor azimuth angle
η_p	Propeller efficiency
θ	Blade pitch angle
Γ	Rotor phase angle
$()_U$	Upper rotor quantity
$()_L$	Lower rotor quantity
$()_0$	Collective component
$()_{1C}$	Longitudinal component
$()_{1S}$	Lateral component
$()_3$	3/rev component
$()'$	Differential trim variable

Presented at the AHS 71st Annual Forum, Virginia Beach, Virginia, May 5–7, 2015.

INTRODUCTION

In recent years there has been much interest in VTOL/hover-capable rotary-wing aircraft that simultaneously have high speed capability. In the high-speed regime, conventional rotary-wing configurations, with rotors operating edgewise, face multiple challenges including compressibility in the advancing blade tip region, stall on the retreating side of the rotor disk, high vibration, and deterioration in rotor performance leading to an eventual inability to produce the required forces. A number of different approaches have been considered to overcome the problems listed above. Tilt-rotor aircraft, for example, reorient the rotors to function as propellers in axial flow while transferring the lifting function to a wing. The V-22 Osprey is capable of achieving flight speeds in excess of 275 kts, but tilt-rotor aircraft have poorer hover performance than a conventional helicopter, a higher empty-weight fraction, and significantly increased complexity (Ref. 1).

While the tilt-rotor may well be the configuration of choice at speeds of 275–300 kts, and upward, slowed-rotor compound and lift-offset coaxial configurations potentially present a better solution at speeds up to around 250 kts. Slowed-rotor compound helicopters reduce the main rotor RPM in high-speed flight to avoid advancing blade compressibility, while mostly transferring their lifting function to wings, and using auxiliary propulsion to provide the required thrust. Lift-offset coaxial configurations, in contrast, use two counter-rotating rotors with each of the rotors generating lift

on its advancing side. They also require auxiliary propulsion at high speeds but eschew the need for a lifting wing. Referred to as the Advancing Blade Concept, shown in Figure 1, lift-offset coaxial rotor technology in high-speed flight was first implemented on the Sikorsky XH-59 helicopter (Refs. 2–7). While the XH-59 was reported to have reached speeds as high as 263 kts, the aircraft experienced high vibration and had poor rotor aerodynamics at high speed. After a hiatus of several years, Sikorsky Aircraft Corp developed a second generation high-speed coaxial rotor aircraft prototype, the X2 Technology^{TM} Demonstrator (Refs. 8–11), which improved on many of the shortcomings of the XH-59. The X2 uses four-bladed rotors (instead of three-bladed rotors on the XH-59), a more optimized blade twist, chord and airfoil distribution, and advanced active vibration control technologies. The X2 technologies are being scaled up for application to the S-97 Raider^{TM}, and to the SB>1 Defiant in response to the Army's JMR program (Refs. 12, 13).

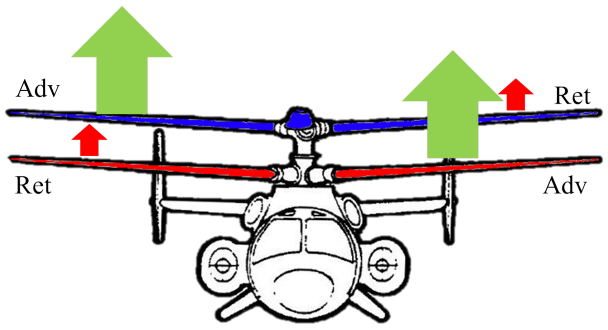

Fig. 1. XH-59 showing advancing blade concept

In addition to the aircraft development efforts undertaken by Sikorsky, a number of researchers in academia and at government labs have also studied high-speed coaxial rotorcraft. Leishman and co-workers have reported on optimum coaxial rotor designs for hover (Ref. 14) and axial flight (Ref. 15) conditions. Rand and Khromov also designed optimum coaxial rotors for hover and axial flight (Ref. 16), as well as high speed cruise (Ref. 17). In Ref. 17 the authors examine the importance of auxiliary propulsion, and also present Pareto frontiers defining minimum power configurations in hover, high-speed flight, and for a combination of the two. A study similar to Ref. 17 was reported by Hersey et al. in Ref. 18.

In Ref. 19, Giovanetti and Hall analyzed coaxial helicopters operating at high speed (250 kts, 0.85 advance ratio), and determined optimum circulation distributions and blade geometries while using higher harmonic blade pitch control. This optimization was conducted at a fixed value of rotor speed. It was shown that the lowest power solutions corresponded to a lift-offset close to 0.5, and constraining the lift-offset to lower values as is commonly done in practice incurs power penalties. Studies on maximum blade loading capability and high-speed performance of coaxial rotorcraft were conducted by Johnson (Refs. 20,21) using CAMRAD II. These studies, also conducted at a single rotor speed, corroborate that performance can be improved with higher lift-offset values. Floros and Johnson showed that slower rotor speeds correspond with a reduction in propulsive power required in Ref. 22. They showed that various types of rotors can remain stable at high forward speeds and advance ratios in Ref. 23.

At the University of Glasgow in the UK, the vorticity transport method was used by Kim and Brown to conduct a high-fidelity analysis of coaxial rotor performance (Ref. 24). The analysis was extended to account for interactions between the rotor wake and the rear mounted propeller (Ref. 25). More recently, Ferguson and Thompson, also at the University of Glasgow, studied the performance and the flight dynamics of high-speed coaxial rotorcraft (Refs. 26, 27).

Over the past decade there has been considerable effort focused on exploiting control redundancies in compound helicopters. Since redundant controls allow numerous possible trim states, a combination of controls can be used to meet one or more objectives such as minimization of power requirement, rotor vibration, rotor flapping, or noise (Refs. 28–33). As in the case of compound helicopters, high-speed coaxial rotorcraft, too, have redundant controls. Coaxial helicopters are equipped with rotor collective pitch and differential collective pitch (which control main rotor thrust and torque), longitudinal cyclic pitch (which produces a pitching moment) and differential longitudinal cyclic (which alters the longitudinal cyclic between the upper and lower rotors), lateral cyclic pitch (which produces a rolling moment and is generally small in steady level flight) and differential lateral cyclic pitch (which influences the rotor lift-offset). Aircraft trim requires satisfaction of force and moment equilibrium about three axes (six equations). Typically, with the differential lateral cyclic selected to achieve a specific lift-offset, four controls (collective, differential collective, longitudinal cyclic, and lateral cyclic pitch) and two aircraft states (pitch and roll attitude) are determined through the solution of the six equilibrium equations. However, propulsor thrust and main rotor RPM are additionally available as control variables, and variation in differential lateral cyclic can be considered as well. This study seeks to examine how control redundancies could be exploited to minimize power requirement and hub vibrations for the XH-59 coaxial rotor helicopter in high-speed flight, with an emphasis on understanding the changes in the underlying physics that produce the benefits.

COAXIAL SIMULATION MODEL

A model of the XH-59 has been developed in the Rotorcraft Comprehensive Analysis System (RCAS) (Ref. 34) with the technical specifications for the aircraft from Felker, Rudell, and Pleasents (Refs. 2, 3, 6). Key properties are summarized in Table 1.

Controls

The XH-59 employs two counter rotating rotors, the upper rotor rotating counter-clockwise and the lower rotating clockwise. Each of the two rotors can independently vary collective

Table 1. XH-59 Aircraft Characteristics

Rotor engines	2 x P&W PT6T-3 turboshaft
Propulsor thrust engines	2 x P&W J60-P-3A turbojet
Fuselage length	40.8 ft
Overall height	12.9 ft
Rotor diameter	36 ft
Rotor separation	2.5 ft
Shaft tilt	0°
CG (fwd of rotor shaft)	5.3 in
CG (below bottom rotor)	3 ft
Nominal rotor speed	345 RPM
Nominal rotor tip speed	650 ft/sec
Blades per rotor	3
Blade precone	3°
Gross Weight (incl. turbojets)	11,900 lb

and cyclic pitch. This gives the rotor system a total of six degrees of freedom. $\theta_{0U}, \theta_{1CU}, \theta_{1SU}, \theta_{0L}, \theta_{1CL}, \theta_{1SL}$, where the subscripts U and L correspond to the upper and lower rotors, respectively. The blade pitch on each individual rotor is given by

$$\theta_U = \theta_{0U} + \theta_{1CU}\cos(\psi_U + \Gamma) + \theta_{1SU}\sin(\psi_U + \Gamma) \quad (1)$$

$$\theta_L = \theta_{0L} + \theta_{1CL}\cos(\psi_L + \Gamma) + \theta_{1SL}\sin(\psi_L + \Gamma) \quad (2)$$

The rotor azimuth angle, ψ, increases in the direction of blade rotation. An azimuthal position of 0°is oriented towards the tail for both rotors. For the counter clockwise upper rotor ψ=90°(advancing side) corresponds to the blade tip pointing to the right of the helicopter as viewed from the top, whereas for the clockwise lower rotor, ψ=90°(also the advancing side) corresponds to the blade tip pointing toward the left of the helicopter as viewed from the top. The XH-59 rotor is very stiff, so the flap response occurs much more quickly than on an articulated rotor. While θ_{1C} is used to produce lateral control for an articulated rotor, it is actually the $\sin(\psi)$ terms that produce lateral control moments on the XH-59 rotor. Similarly, the $\cos(\psi)$ terms produce longitudinal moments, rather than the $\sin(\psi)$ terms, as in an articulated rotor. Γ is the phase offset, which serves to offset the azimuthal location in which the blade pitch is applied. Rather than keep the same nomenclature as an articulated rotor and set Γ close to -90°, the degrees of freedom are re-cast in terms of new variables which can also make the overall state of the rotor system easier to grasp. The new variables are the same as those described in Refs. 2 and 6 and are shown in Table 2.

Table 2. Rotor control variables

Collective	θ_0	$= \frac{1}{2}(\theta_{0U} + \theta_{0L})$
Differential collective	$\Delta\theta_0$	$= \frac{1}{2}(\theta_{0U} - \theta_{0L})$
Longitudinal	A_1	$= -\frac{1}{2}(\theta_{1CU} + \theta_{1CL})$
Differential longitudinal	A_1'	$= -\frac{1}{2}(\theta_{1CU} - \theta_{1CL})$
Lateral	B_1	$= -\frac{1}{2}(\theta_{1SU} - \theta_{1SL})$
Differential lateral	B_1'	$= -\frac{1}{2}(\theta_{1SU} + \theta_{1SL})$

With these new variables, the pitch on the upper and lower rotors is given by

$$\theta_U = \theta_0 + \Delta\theta_0 - (A_1 + A_1')\cos(\psi_U + \Gamma) - (B_1 + B_1')\sin(\psi_U + \Gamma) \quad (3)$$

$$\theta_L = \theta_0 - \Delta\theta_0 - (A_1 - A_1')\cos(\psi_L + \Gamma) + (B_1 - B_1')\sin(\psi_L + \Gamma) \quad (4)$$

The collective pitch, θ_0, now represents the average collective pitch of both rotors, while the differential collective, $\Delta\theta_0$, represents the difference in collective pitch of the upper and lower rotors from the average. The lateral pitch, B_1, represents pitch that is high on the left side of the helicopter and will cause a rightward roll moment. The longitudinal pitch, A_1, represents pitch that is high on the front of the helicopter and will cause a nose-up moment. A positive differential lateral pitch, B_1', represents increased pitch on the retreating sides of both rotors, and a negative value will increase pitch on both advancing sides. A positive value of differential longitudinal pitch, A_1', represents higher pitch on the front of the upper rotor, and on the back of the lower rotor. The differential longitudinal pitch is kept at zero or low values in the flight tests in Ref. 2 and is set to zero in all of the current simulations. The phase offset used in the high speed flight testing (Refs. 2, 5) and current simulations is Γ = 40°. This value helps correct for the delayed response of the blades which, even though being stiff, have some flexibility.

Main Rotor Blades

The XH-59 has two 3-bladed rotors. Each blade is attached to the hub with a single pitch bearing. The blades have a 3°precone angle, and are linearly tapered. The aerodynamic sections of the blade begin at 20% span. The chord decreases from 20.7 in at 20% span to 11.5 in at the blade tips. The blade twist distribution is shown in Figure 2. RCAS models the rotor blades as elastic beams undergoing coupled flap bending, lag bending, and elastic torsion. The stiffness and mass properties are taken from Ref. 2. The blade was discretized using 10 equal length structural finite elements. The blades were modeled using several different airfoil sections, as indicated by Figure 3, which shows the thickness distribution as a percent of chord.

The airfoil sections used in the simulation and shown in Figure 3 are different from the actual airfoil sections on the XH-59; the actual airfoils used were the NACA 63(230)-224A, NACA 63(230)-213A and NACA 23012(64), as reported in Ref. 3. The data for these sections was not available, so the similar NACA 0026, 63-218, and 23012, for which tables of the sectional lift, drag, and moment coefficients were available, were used. These are the same sections used to model the XH-59 in Ref. 6. While Ref. 6 applied the 3 aerodynamic tables to 3 distinct sections of the blade (inner, middle, and outer), the current model blends the data smoothly to represent the smooth variation of the the actual blade. Figure

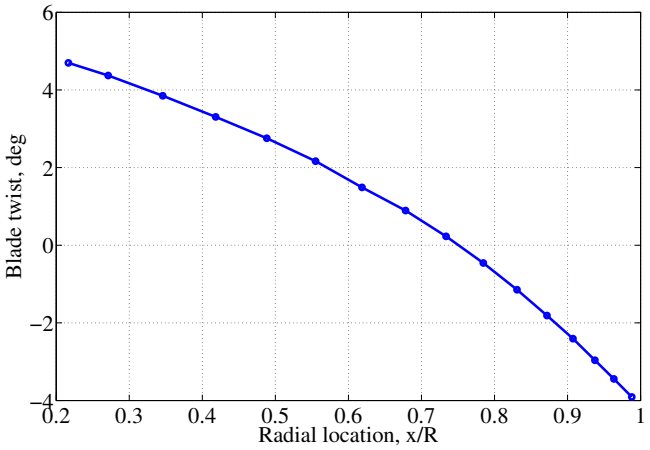

Fig. 2. Blade twist distribution

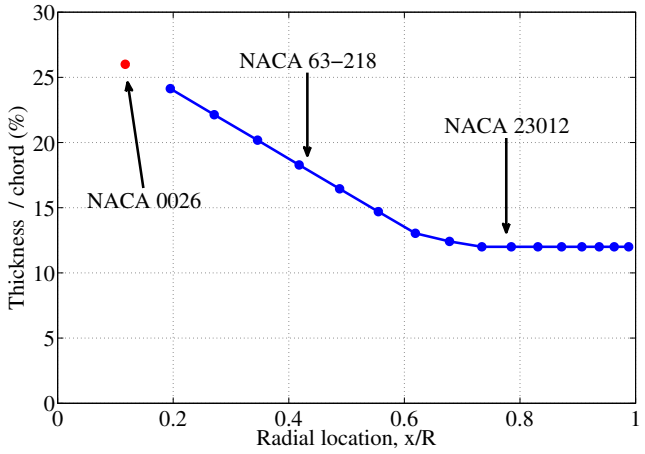

Fig. 3. Blade thickness distribution and airfoils

3 shows that the blade sections taper in thickness to chord ratio from 26% to 12%. To re-create this effect, intermediate airfoil tables were created by interpolating between the airfoil section coefficients, based on airfoil thickness to chord ratio, between the 26% thick NACA 0026, the 18% thick NACA 63-218, and the 12% thick NACA 23012 (so each table matches the actual blade thickness where it is applied). There were 16 total aerodynamic sections used to model the blade, shown as the blue dots in Figure 3. The red point in Figure 3 marks the point where the NACA 0026 would be.

Fuselage

The fuselage aerodynamic coefficients were obtained from the full-scale wind tunnel test data in Ref. 3 and the scaled down wind tunnel tests in Ref. 4. This data was used to construct fuselage lift and pitching moment coefficients that varied linearly with angle of attack and a fuselage drag coefficient that varied quadratically with angle of attack. The fuselage aerodynamic coefficients included the effect of the hub, horizontal tail, and vertical stabilizers. The aircraft gross weight (11,900 lbs) and geometry, including locations of the center of gravity, rotors, and auxiliary jet engines were obtained from Ref. 2. The propulsive force, representing the thrust of the two J60 engines, was applied as a point force at the engine attachment point.

Rotor Inflow

Initial simulations exercised both the Peters-He finite-state wake, as well as a prescribed vortex wake models. The Peters-He inflow yielded faster convergence over more cases with little difference in overall power and control predictions. The results presented use an 8×8 state wake. Increasing the number of states to 19×19 and comparing the methods at the baseline trim state resulted in less than 1% change in total power, less than 6% change in rotor H-force, and less than 3% change in 3P vibratory force and moment magnitudes. Comparing a prescribed wake model to the 8×8 state dynamic inflow also resulted in less than 1% difference in total power predictions. The prescribed vortex wake was able to capture finer details of the blade vortex interactions, and resulted in higher predictions for the 3P vibration magnitudes, however the vibration trends with airspeed were captured even with the faster finite-state wake model.

Analysis

The total power of the vehicle is computed by adding the main rotor power and the power required by the auxiliary jet engines.

$$P_{\text{total}} = P_{\text{rotor}} + \frac{TV_{\infty}}{\eta_p} \tag{5}$$

The propulsive power is computed using an estimated propeller efficiency, η_p. The efficiency of the J-60 jet engines operating at 250 kts is estimated to be 0.7. Using a propulsion method more appropriate to the current speed range of 250 kts, such as a propeller, could improve the efficiency. (Ref. 21 used η_p = 0.9 for a similar study with a propeller). In the high speed regime, the power required by the propulsor will be significantly larger than the main rotor power, even for a very efficient propulsor.

The rotor H-force, or rotor drag, is the overall drag produced by the rotor system. The rotor drag is found by taking the sum of the components of the drag, dD_c, in the chordwise direction on each blade section in the x-direction (towards the rear of the aircraft).

$$dF_x = dD_c \sin(\psi) \tag{6}$$

The blade drag approaching ψ=90°and ψ = 270°is the dominant contributor to the overall rotor drag.

Another important parameter is the rotor lift-offset, which can be thought of as the lateral location of the center of lift of each rotor (Ref. 20). It is calculated as

$$LOS = \frac{\Delta M_x}{TR} \tag{7}$$

where ΔM_x is the difference between the lateral moments between the upper and lower rotor, T is the combined thrust of the two rotors, and R is the rotor radius.

Becuase the XH-59 rotors are 3-bladed, the 3/rev components of the rotor blade forces and moments are passed through the hub and felt as vibrations in the rest of the aircraft. The magnitude of the 3/rev vibratory hub forces and moments are given by

$$F_3 = \sqrt{F_{x3}^2 + F_{y3}^2 + F_{z3}^2} \tag{8}$$

$$M_3 = \sqrt{M_{x3}^2 + M_{y3}^2} \tag{9}$$

Where F_{x3}, F_{y3}, and F_{z3} are the longitudinal, lateral, and vertical component of the 3/rev vibratory hub forces and M_{x3} and M_{y3} are the 3/rev vibratory rolling and pitching moments.

Validation

Figure 4 shows RCAS predictions of aircraft power requirement versus airspeed, compared to flight test data from Refs. 2 and 5. The simulations at high-speed include the use of auxiliary propulsion, while the simulations at low speed (below 100kts), have the auxiliary thrust set to zero. The values of differential lateral cyclic and main rotor RPM were matched to those used in the flight test. Figure 4 shows that the power predictions using RCAS compare well to the flight test data.

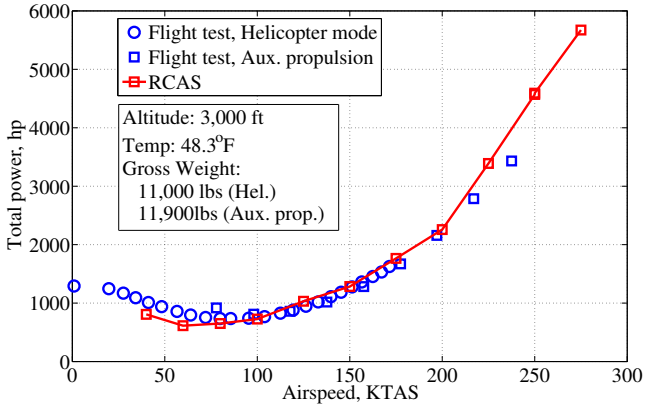

Fig. 4. RCAS simulation of XH-59 power requirement versus airspeed compared to flight test data

Coaxial rotors have unique vibration characteristics. The counter rotating rotors actually provide cancellation of some components of the vibratory loads. O'Leary and Miao provide a comprehensive description of this cancellation and investigate vibratory loads on the XH-59 in Ref 7. The current simulations use a blade crossover angle of $\psi = 0°$, meaning the blades of the upper and lower rotor cross directly over each other at 0°azimuth (directly over the tail). Flight tests in Ref. 2 explored both 0°crossover and 90°crossover, and found that 0°crossover resulted in more favorable performance. Figure 5 shows the 3P vibratory hub moments at 250 kts, rotor at 97% nominal speed, and $B_1' = 2.5°$compared with flight test measurements. The lateral (roll) moments are small compared to the longitudinal (pitch) moments. Because the majority of longitudinal hub moments are generated by blade lift at $\psi = 0°$and $\psi = 180°$(when the upper and lower blades are in the same location) the longitudinal (pitching) vibratory moments are large. The lateral moments are generated mostly by the blade lift near $\psi = 90°$, and are opposite in direction between the upper and lower rotors. Because both the upper and lower rotors encounter their respective advancing side at the same time, the lateral vibratory moments cancel out, resulting in the low magnitude shown in Figure 5. Although the magnitudes of the vibrations between the dynamic wake, prescribed wake, and flight testing differ by some margin, the trends with airspeed (not shown in the paper) and cancellation characteristics are captured in the analysis.

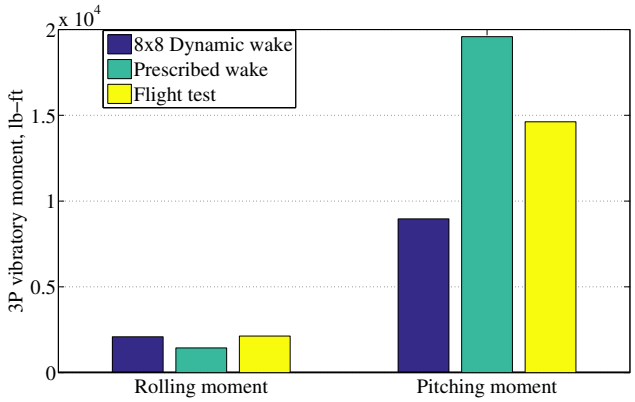

Fig. 5. RCAS predictions of 3P vibratory moments compared to flight test data

RESULTS

RCAS simulations for the XH-59 were undertaken at a forward flight speed of 250 kts, based on the Army JMR specification. The simulations were carried out at 3,000 ft altitude and temperature of 48.3°F, which corresponded to a density of 0.002175 slug/ft^3. Six vehicle equilibrium equations are used to solve for the following six aircraft trim variables: collective pitch, differential collective pitch, longitudinal cyclic pitch, lateral cyclic pitch, and aircraft pitch and yaw attitude. After setting differential longitudinal pitch to zero, three additional controls remain: rotor RPM, auxiliary thrust, and differential lateral pitch. The rotor speed was allowed to vary from the nominal value of 345 RPM down to 196 RPM (57% of nominal). Additionally the differential lateral pitch, B_1', was varied from 2.5°to -7°. At each combination of rotor speed and differential lateral pitch, the aircraft was trimmed with varying levels of propulsor thrust. Figure 6 shows a schematic of the horizontal forces occurring on the aircraft. Figure 7 shows the total power required as the propulsor thrust is varied for a few selected cases.

It is observed that as propulsor thrust is reduced, the total

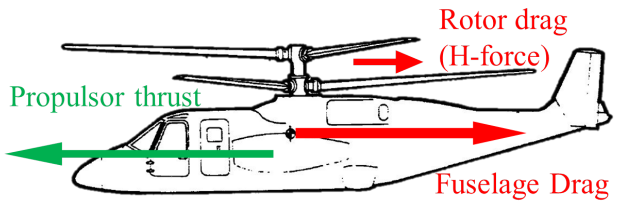

Fig. 6. Diagram of horizontal forces on aircraft

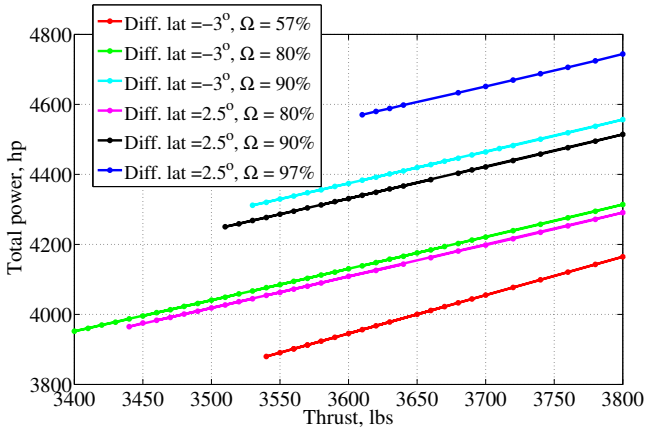

Fig. 7. Relationship between propulsor thrust and power

power decreases. This is due to the propulsive power being the dominant component of the total power. The propulsor thrust can only be reduced to a certain amount, below which, the aircraft is incapable of trim. Propulsor thrust reduction corresponds with the vehicle angle of attack moving from slightly positive ($< 1°$) towards zero. All of the simulation results presented in this paper correspond to minimum possible propulsor thrust. The reason for the existence of a minimum value of propulsor thrust is because beyond a certian point, it is unable to overcome the fuselage and rotor drag. At moderate speeds, it is possible for the the vehicle to trim with low propulsor thrust by tilting to a nose-down pitch attitude and allowing the rotor to supply some of the necessary propulsive force, but this could not be demonstrated at high speeds because the fuselage and rotor drag are too large.

Similar to Figure 7, 3/rev vibration levels were examined versus propulsor thrust and found to be insensitive to propulsor thrust variation. Using the minimum possible propulsive thrust which allows aircraft trim leaves only two additional variables to consider, rotor RPM and rotor differential lateral pitch and makes visualization easier.

Figures 8 and 9 show the total power required and the magnitude of the rotor hub vibratory forces, respectively, as a function of rotor RPM and differential lateral pitch. Marked on the figures is the point BL (baseline) which corresponds to 97% nominal RPM and 2.5 deg differential lateral pitch used in the flight tests reported in Ref. 2. On Figure 8, it is observed that the lowest power is at the operating state corresponding to 65% nominal RPM and a differential lateral cyclic of -3°, and this point is marked as LP (low power). On Figure 9, however, it is observed that the vibratory forces at the low power state are very high. The point marked LV (low vibration) is at 70% nominal RPM and the same differential lateral cyclic (-3°) as the low power state. This point has a power requirement that is only marginally higher than at the low power state, but with substantially reduced hub vibratory forces. Note that the point marked LV does not correspond to minimum vibration, but rather an operating state that results in low vibration while requiring close to minimum power. The total power corresponding to the low vibration and low power states are 83.11% and 83.35%, respectively, of the value at the baseline trim state (details for the three states given in Table 3).

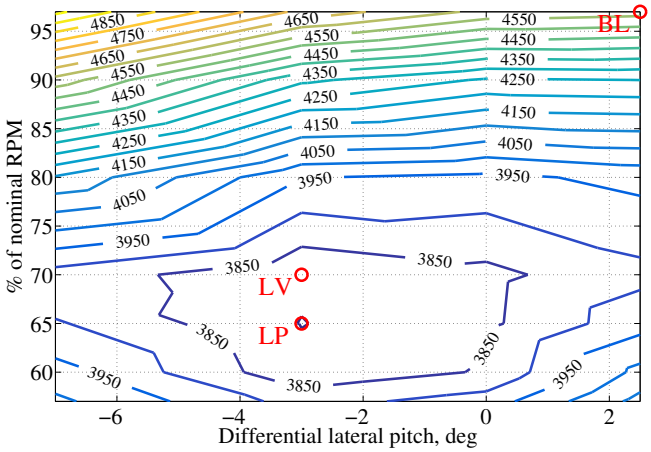

Fig. 8. Total power, hp

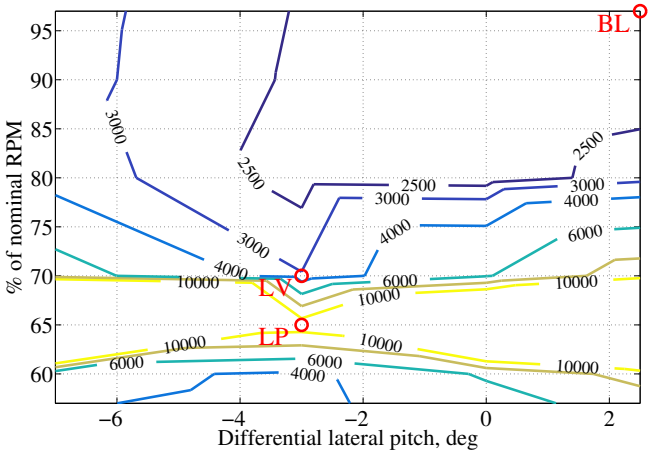

Fig. 9. 3P vibratory force magnitude, lbs

In Table 3 the aircraft pitch attitude is defined as positive nose-up, but the vehicle is seen to trim at near-zero pitch attitude (nose-level) in all cases. The negative longitudinal flapping values indicate that the rotor experiences a slight blowback. One of the contributions to reduction in main rotor power for the low power and low vibration cases is reduction in profile power associated with reduction in rotor RPM

Table 3. Comparison of trim states, 250 kts

	BL	LV	LP
Rotor speed (% of Nr)	97%	70%	65%
Advance Ratio	.67	.93	1.0
Advancing tip Mach no.	0.95	0.79	0.76
Lift-offset	.233	.395	.402
Collective pitch (θ_{75})	5.73°	2.79 °	3.37°
Longitudinal pitch	-3.11°	-0.21°	-0.48 °
Differential lateral pitch	2.5°	-3°	-3°
Aircraft pitch attitude	0.004°	-0.012°	0.001°
TPP angle of attack (upper)	0.79°	1.03°	1.09°
TPP angle of attack (lower)	0.55°	1.06°	1.14°
Lon. flapping (upper)	-0.78°	-1.05°	-1.09°
Lon. flapping (lower)	-0.55°	-1.08°	-1.14°
Lateral flapping (upper)	0.56°	2.03°	2.19°
Lateral flapping (lower)	0.60°	2.09°	2.26°
Propulsor Thrust (lbs)	3610	3390	3430
Fuselage drag (lbs)	2763	2763	2763
Rotor H-force (lbs)	851.5	621.2	659.1
Reverse flow H-force	11.2%	8.2%	9.3%
Total Power (hp)	4570	3809	3798
Propulsor Power (hp)	3956	3715	3759
Main Rotor power (hp)	613.8	93.6	39.3
Reverse flow Power	-5.8%	-6.1%	-7.4%
Forward flow Power	105.8%	106.1%	107.4%
3P force (lbs)	2309	3032	11074
3P moment (lb-ft)	9201	9269	62507

from 97% nominal for the baseline case to 65–70%. In addition, for the low vibration and low power cases the slightly larger blowback of the rotor tip-path place (a more negative longitudinal cyclic flapping) results in a larger component of the incoming airstream associated with the forward velocity of the aircraft presenting itself as an upwash and putting the rotor in a near autorotative state. For the low vibration and low power trim states, which have higher pitch on the advancing side (due to negative differential lateral) both the upper and lower rotors experience a greater tilt towards their retreating sides, as indicated by the larger lateral flapping values in Table 3 (lateral flapping is defined in this study as positive for rotor tilting to the retreating side). The flight tests in Ref. 2 were flown with a positive differential lateral pitch to limit the lift-offset.

Performance

Figures 10 and 11 show the main rotor and propulsor power, respectively, over the range of rotor RPM variation and differential lateral cyclic considered. It is immediately evident that the main rotor power is a small fraction of the total power while the propulsor power is the dominant component. The rotor power constitutes less than 15% of the total power in all of the cases tested. The main rotor power requirement (Fig. 10) reduces with RPM reduction, while the propulsor power variation (Fig. 11) broadly corresponds to that seen in total power (Fig. 8). In theory, the rotor could operate in a negative power state (i.e. the rotor is extracting power as in a windmill) however, in this analysis, any negative rotor power (generated by the rotor as opposed to consumed) is neglected and the rotor power is set to zero. This is because most helicopters are not equipped to extract and use power from the rotor. From Table 3, the main rotor power for the baseline state is 13.43% of the total power, and for the low power and low vibration states, the corresponding values are 1.03% and 2.46%, respectively.

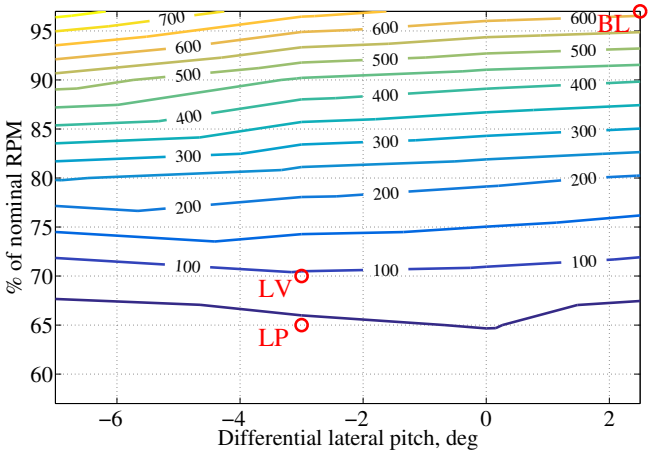

Fig. 10. Main rotor power, hp

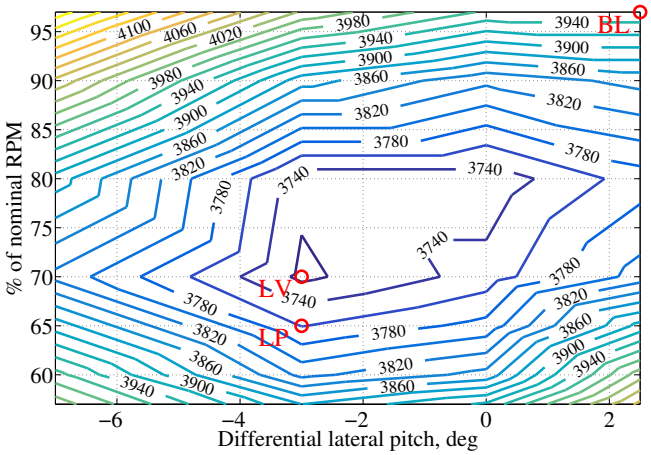

Fig. 11. Propulsor power, hp

It is observed in Table 3 that the longitudinal cyclic flapping of both the upper and lower rotors (for all three states, baseline, low power, and low vibration) has negative values. With the aircraft pitch attitude for all three cases being nearly nose level, the blow back of the rotor disk, in combination with the high operational speed, produces a strong upwash through the rotor disk putting it in partial autorotative descent like conditions, accounting for the low power. This blow back of the rotor disk is seen to be stronger for the low vibration and low power cases in Table 3, consistent with the reduced main rotor power for these cases.

Figures 12 and 13 show rotor H-force and propulsor thrust, respectively, varying with rotor RPM and differential lateral

cyclic. The propulsor thrust, of course, is the propulsor power plot (Fig. 11) scaled by the flight speed of 250 kts and propeller efficiency, and its variation appears qualitatively similar to the total power plot (Fig. 8), as well, since the propulsor power is the major contributor to total power. Although the minimum rotor H-force is observed in Fig. 12 at differential lateral cyclic values closer to 1°, the values at 3°, 65–70% nominal RPM (corresponding to the low power and low vibration trim states) remain fairly close to the minimum, and much lower than the H-force at the baseline trim state (values given in Table 3).

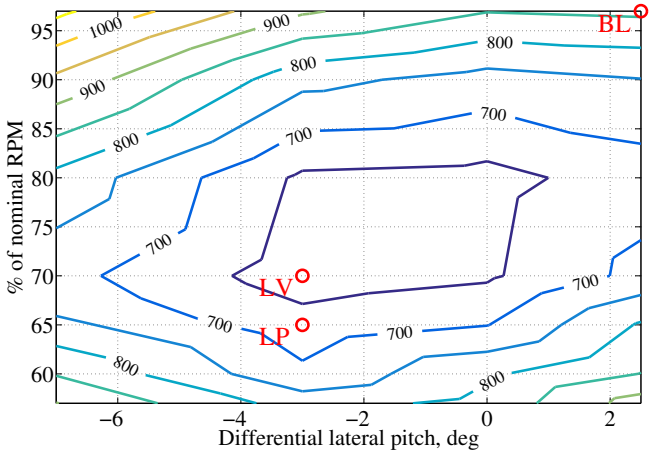

Fig. 12. Rotor H-force, lbs

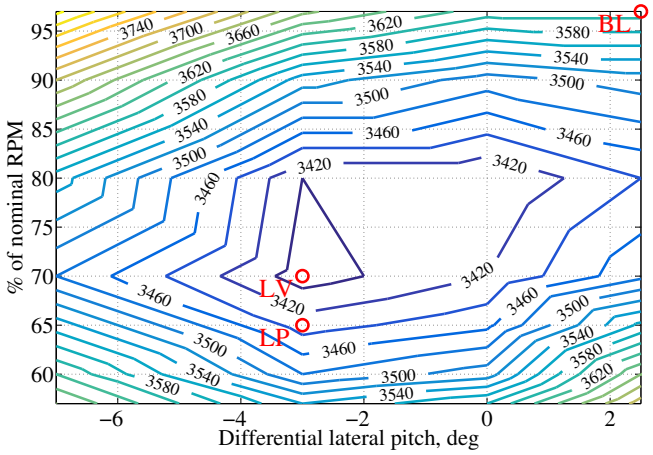

Fig. 13. Propulsor thrust, lbs

Figure 14 shows a plot of the rotor lift-offset, which is seen to increase as the rotor RPM decreases and as the differential lateral cyclic goes from positive values through zero to negative values. At the low power and low vibration trim states, where total power requirement is about 17% lower than at the baseline state, the rotor lift-offset is nearly 40%, significantly higher than the 23.3% at the baseline state. In practice, the lift-offset is often limited to a small value (30% in the case of the X2 (Ref. 8)) in order to limit the size of the hub, avoid excessive blade bending moments, and avoid upper/lower blade tip strike. Depending on the specifics of the rotor design and constraints on blade loads, higher rotor lift-offset may indeed preclude operation at minimum power conditions.

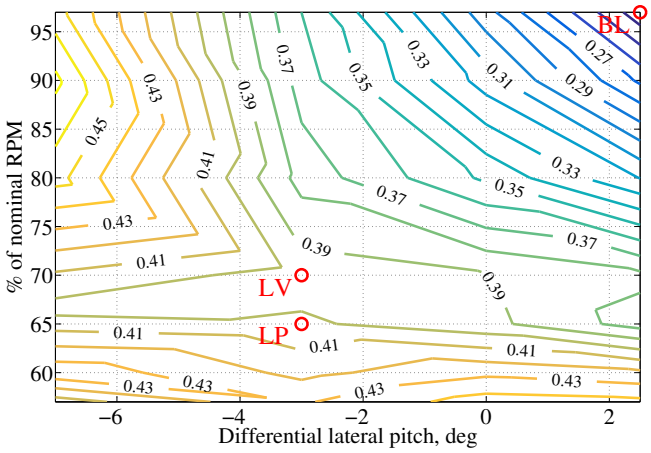

Fig. 14. Rotor lift-offset

Vibration

Figures 15–17 show the longitudinal, lateral, and vertical components of the 3/rev vibratory hub forces, respectively. The lateral vibratory hub forces are seen to be substantially lower in magnitude than the longitudinal forces, expected in the present case for blade crossover at $\psi = 0°$. The peak longitudinal vibratory forces are also greater than the vertical forces, and are the dominant contributors to the total 3/rev hub vibratory forces presented in Figure 9. Figure 18 (Ref. 2) shows the rotor fan plot for the XH-59 and it is evident that while the first flap and first chord modes are well separated from the 2/rev line at the nominal rotor speed, the two modes converge and approach the 2/rev line as the rotor RPM reduces to 70% nominal. It is expected that first flap and chord the mode frequencies would get even closer to 2/rev at 65% nominal RPM and proximity to resonance results in a large increase in vibratory forces. This is seen in Figure 9 and the rest of the vibration plots as a band of high vibration magnitudes around 65% rotor speed. The lateral and longitudinal vibratory forces are influenced more significantly than the vertical forces, as they are more sensitive to 2/rev excitations. In Table 3 the 3/rev vibratory forces at the low power state are 4.8 times larger than at the baseline, but increasing from 65% to 75% nominal rotor RPM to the low vibration state, and moving away from resonance slightly, the vibratory forces reduce to only 1.31 times the value at baseline. As stated earlier, The 3P hub forces and moments do not vary significantly with different propulsor thrust applied, so the results in figures 15–17 are representative of the values at trim conditions with greater propulsor thrust as well.

Figures 19–20 show the 3/rev vibratory pitching and rolling moments at the rotor hub, respectively, and Figure 21 shows the combination of hub pitching and rolling moments.

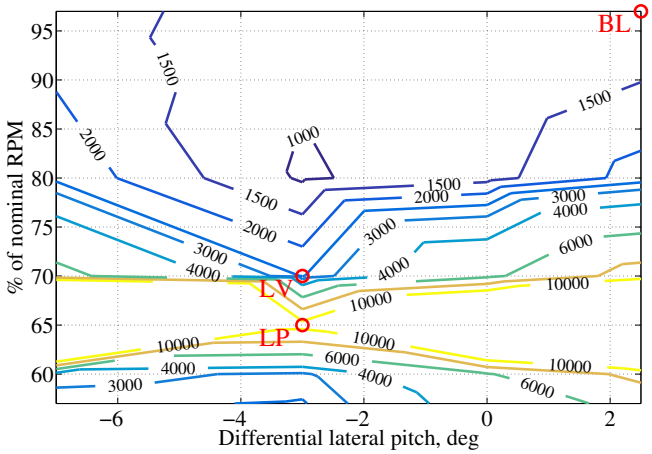

Fig. 15. 3P longitudinal vibratory force, lbs

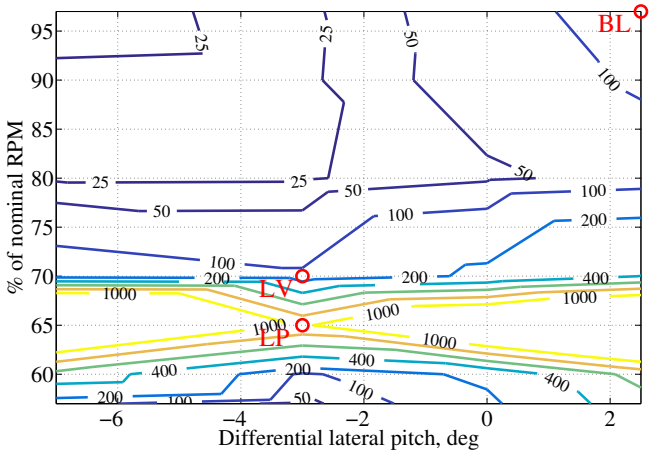

Fig. 16. 3P lateral vibratory force, lbs

Due to the blade crossover at $\psi = 0$ deg, the magnitude of the rolling moments are very small compared to the pitching moments. As with the 3/rev vibratory hub forces in Figure 9, a peak in 3/rev vibratory moments is observed at reduced rotor speeds. In Table 3, the vibratory moments at the low power state are predicted to be 6.79 times higher than the baseline, but increasing the RPM from 65% to 70% nominal RPM moves the system sufficiently away from resonance so that vibratory moments at the low vibration state are almost comparable to the levels at baseline.

Examination of baseline trim state

Figure 22 shows the upper and lower rotor pitch variation, versus azimuth, at 75% radius for the baseline, low power, and low vibration trim states. The pitch variation for the baseline state with a +2.5°differential lateral cyclic differs considerably from the low power and low vibration states with a -3°differential lateral pitch. While the pitch on the advancing side increases by about 2° from the baseline case to the low power and low vibration cases, the pitch on the retreating side decreases by as much as 7°. The baseline case also trims with

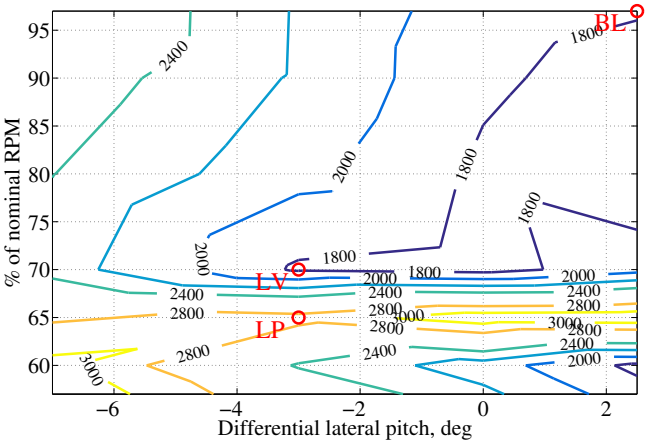

Fig. 17. 3P vertical vibratory force, lbs

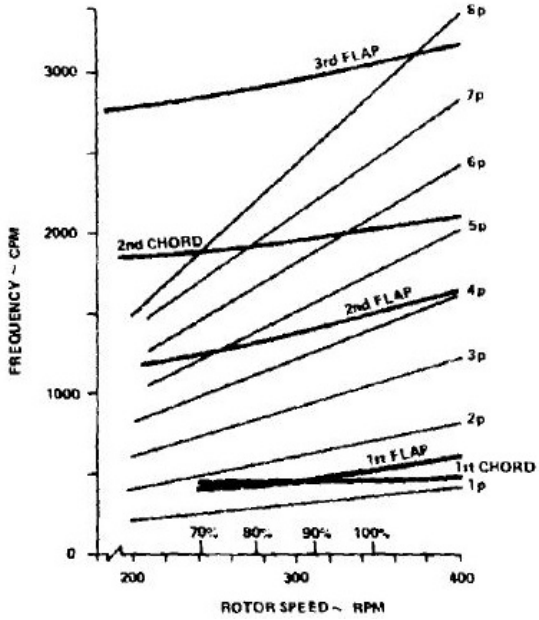

Fig. 18. Rotor fan plot (Ref. 2)

a -3.1°longitudinal pitch, which, because of the 40° phase offset, acts in addition to the positive differential lateral pitch to increase blade pitch on the retreating sides. The states with negative differential lateral pitch show significantly more lateral flapping. Blade strike was avoided by a significant margin in these cases, as well as all of the states analyzed. For the baseline trim state, Figure 23 shows the angle of attack distribution on disk plots for both the upper and lower rotors. The advancing blade tip is observed to have negative angles of attack (the red contour separates positive from negative regions) and the angles of attack in the reverse flow region are close to 180°. For clarity, all angles of attack above 20°are colored yellow.

Figure 24 schematically represents the aerodynamic state of two blade sections at $\psi = 270°$(viewed from the tip of the blade). The section at 25% span, in the reverse flow region has a geometric pitch of 194°relative to the tangential compo-

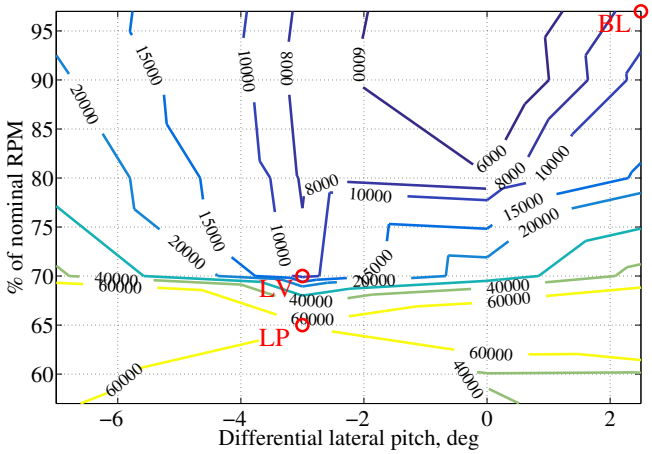

Fig. 19. 3P vibratory pitching moment, lb-ft

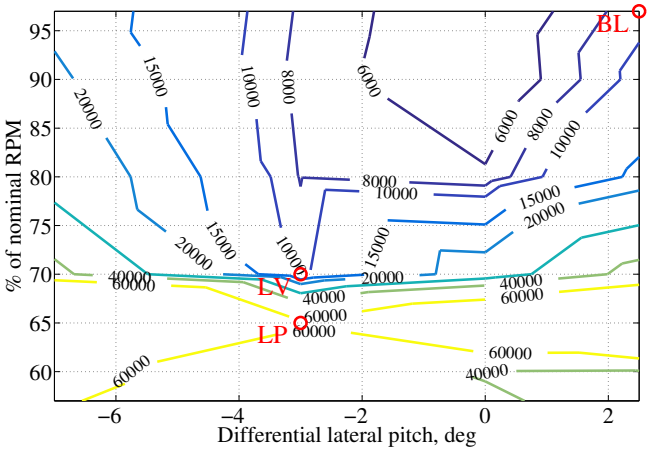

Fig. 21. 3P vibratory moment magnitude, lb-ft

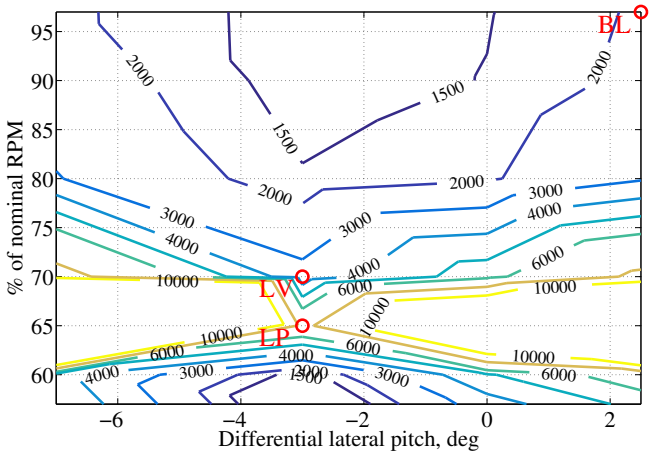

Fig. 20. 3P vibratory rolling moment, lb-ft

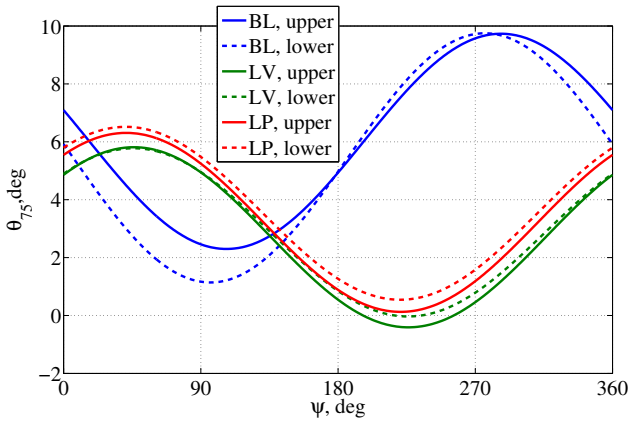

Fig. 22. Blade pitch for selected cases at 250 kts

nent of velocity, and produces negative lift and negative drag (oriented from airfoil trailing edge to leading edge). The section at 85% span, on the other hand, is outside the reverse flow region, has a geometric pitch of 8°relative to the tangential component of velocity, and produces positive lift and drag. Figures 25 and 26 show the lift and drag distribution on rotor disk plots for both the upper and lower rotors, for the baseline case. The reverse flow region is marked by the white dashed circle. Negative lift at the advancing blade tip and in the reverse flow region is clearly observed on Figure 25, while the highest positive lift generating regions are inboard on the advancing side.

On Figure 26 the advancing blade tip is seen to be the dominant contributor to drag (and indeed, to main rotor torque and power requirement). The drag in the reverse flow region is observed to be negative which implies that it actually reduces main rotor torque and power requirement and assists in spinning the rotors. In portions of the disk that appear to have negative drag outside the reverse flow region, the drag is actually very close to zero. The low negative values are attributed to the upwash through the disk associated with the small rearward tilt of the rotor disk. Figure 27 shows disk plots of blade sectional contribution to rotor H-force. Obviously when the blades are at $\psi = 0°$or 180°, the chordwise drag at those azimuthal stations has no contribution to rotor H-force. The greatest contribution to rotor H-force is from the advancing blades, especially from the tip region. However, the negative drag in the reverse flow region that was beneficial for main rotor torque and power is oriented such as to increase the rotor H-force. This, in turn, increases the propulsor thrust requirement. In the baseline case, 11% of the total H-force comes from the reverse flow region, as indicated in Table 3.

Examination of low vibration trim state

The low vibration state is examined in detail in order to compare it to the baseline state. A detailed examination of the low power state is not given, as it was very similar to the low vibration state. Figures 28 and 29 show the angle of attack and lift distribution, respectively, on disk plots for both the upper and lower rotors for the low vibration case. Since the RPM is reduced to 70% nominal, the advance ratio increases to 0.91 (from 0.67 at the baseline RPM) and the reverse flow region (marked by the white dashed circle) is seen to expand accordingly.

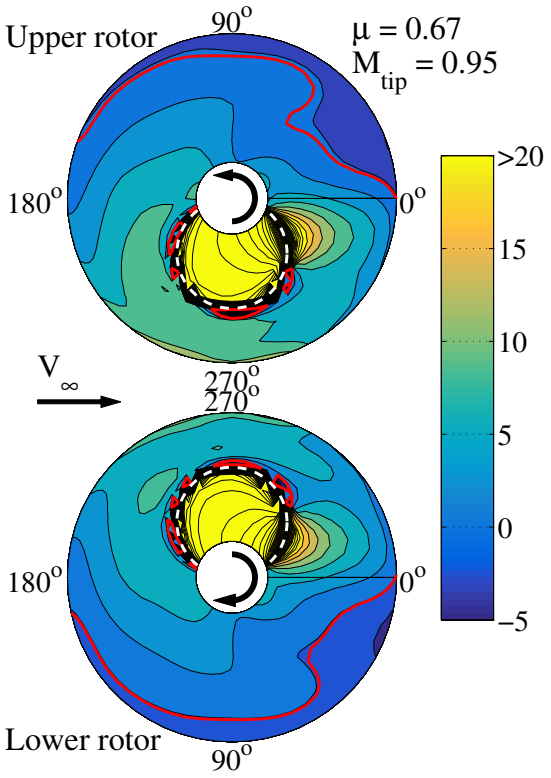

Fig. 23. Baseline state, 97% nominal RPM $B_1' = 2.5°$: Angle of Attack, deg

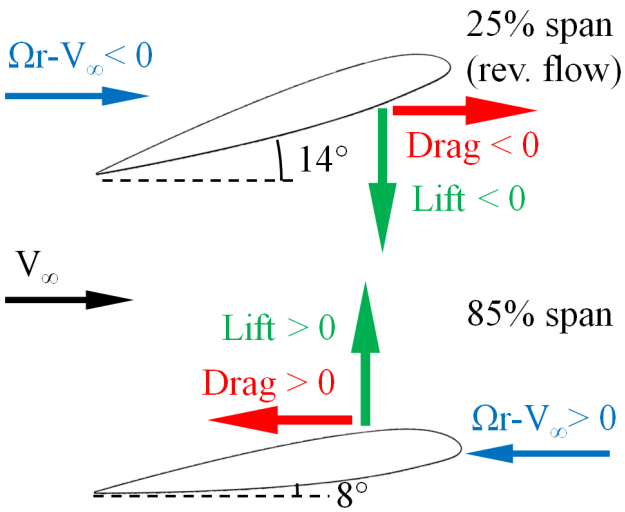

Fig. 24. Blade sections at 25% span (top) and 85% span (bottom) at $\psi = 270°$, Baseline case

Comparing the low vibration angle of attack distribution in Figure 28 to the baseline distribution in Figure 23, negative angles at the blade tip between $\psi = 45°$–$90°$are eliminated, while regions of negative angles of attack are seen to emerge between $\psi = 300°$–$360°$. This change is best understood by examining the rotor pitch variation in Figure 22. From $\psi = 45°$–$90°$the rotor pitch for the low vibration state is higher than the baseline, eliminating the negative angles at the tip. Conversely, in the fourth quadrant, the rotor pitch for the low vibration state is much lower than the baseline. Comparing the lift distribution for the low vibration case in Figure 29 to the baseline case in Figure 25, the negative lift on the advancing blade tip is reduced while a little more negative lift is apparent at the rear of the rotor disk in the blade tip region. These changes are consistent with the changes in angles of attack discussed above. The largest positive lift generating region on the advancing side in Figure 29 is a little further outboard compared to Figure 25, and centered around an azimuthal position closer to $\psi = 90°$. These changes result in the increase in lift-offset for the low vibration case compared to the baseline, reported in Table 3 and Figure 14. While the overall lift generated is similar to the baseline (required to carry the weight of the aircraft), this is generated at lower dynamic pressure associated with reduced rotor speed in combination with higher blade pitch on the advancing side than in the baseline trim state. Also seen on Figure 29 are areas of negative lift in the reverse flow region. Perhaps more interestingly, there appear to be areas of positive lift, even in the reverse flow region (the areas between the solid red and the dashed white lines on the retreating side, in Figure 29). This is best understood from Figure 30 which schematically represents the aerodynamic states at 25% and 85% span at $\psi = 270°$(viewed from the tip of the blade). Recall from Figure 22, that at $\psi = 270°$, the blade pitch for low vibration is much lower than the the baseline. Considering the negative twist of the blade, the outboard 85% section is at a negative pitch and therefore produces positive lift, even in reverse flow.

Figure 31 shows the drag distribution on rotor disk plots for both the upper and lower rotors, for the low vibration state. The advancing blade tip Mach number is reduced considerably for the low vibration case (from 0.95 for the baseline state down to 0.79). Comparing Figures 26 and 31 and 27 and 32, it is evident that the drag divergence at the tip has been eliminated. The highest values of drag move inboard on the advancing blade where the maximum lift is generated. This inboard movement of the drag, in addition to reduction in peak value, reduces main rotor torque and power requirement. Negative drag observed in the reverse flow region, also reduces main rotor torque and power requirement. Also seen are areas of negative drag outside of the reverse flow region. This is attributed to the increased blowback of the rotor disk resulting in an upwash through the disk from the forward velocity of the aircraft and bringing it closer to an autorotative state. Figure 32 shows disk plots of contribution to rotor H-force for the low vibration case. The greatest contribution to rotor H-force is from the advancing blades, but from the mid-span region of the blade where drag is the highest. The negative drag on the retreating side that reduces main rotor torque and power is still a contributor to the rotor H-force. Although the reverse flow region has grown considerably, the lower blade pitches on the retreating side due to the negative differential lateral keep the reverse flow H-force small, only 8.2% of the total rotor H-force.

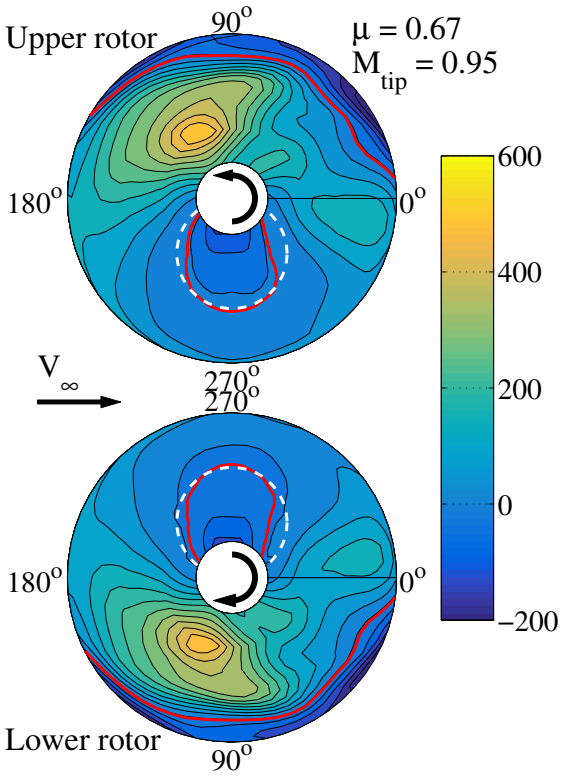

Fig. 25. Baseline state, 97% nominal RPM $B_1' = 2.5°$: Blade lift, lbs/ft

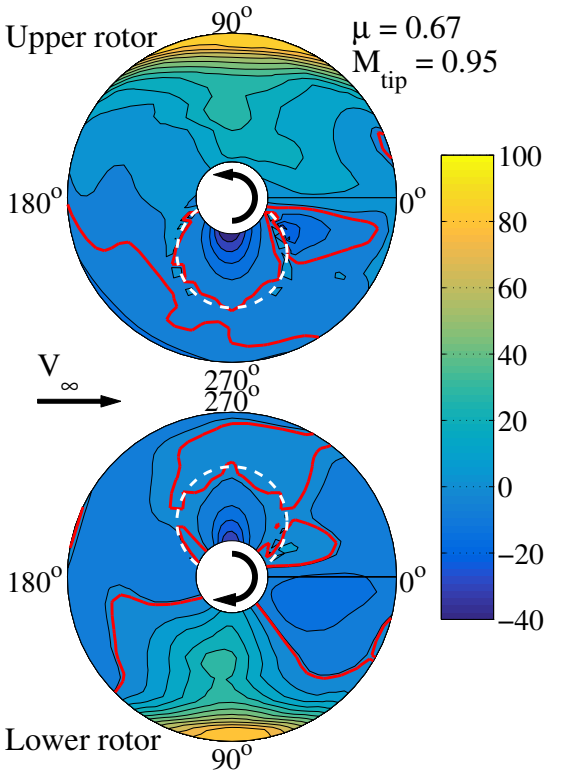

Fig. 26. Baseline state, 97% nominal RPM $B_1' = 2.5°$: Blade drag, lbs/ft

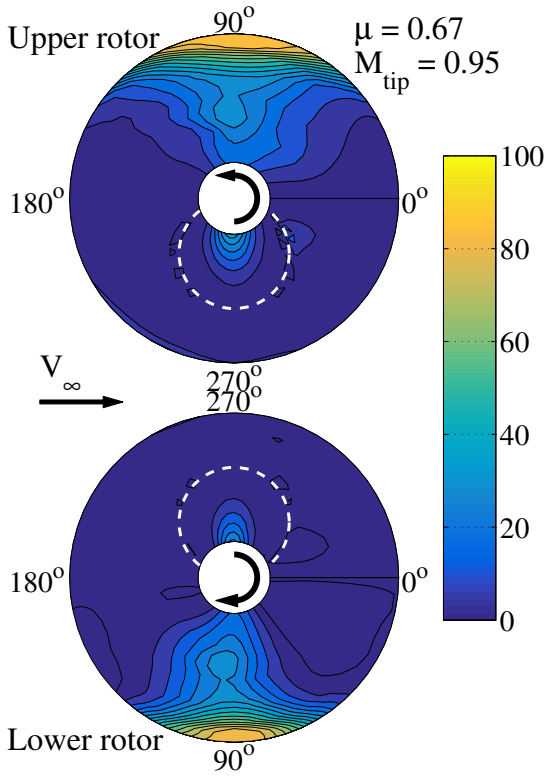

Fig. 27. Baseline state, 97% nominal RPM $B_1' = 2.5°$: Blade H-force contribution, lbs/ft

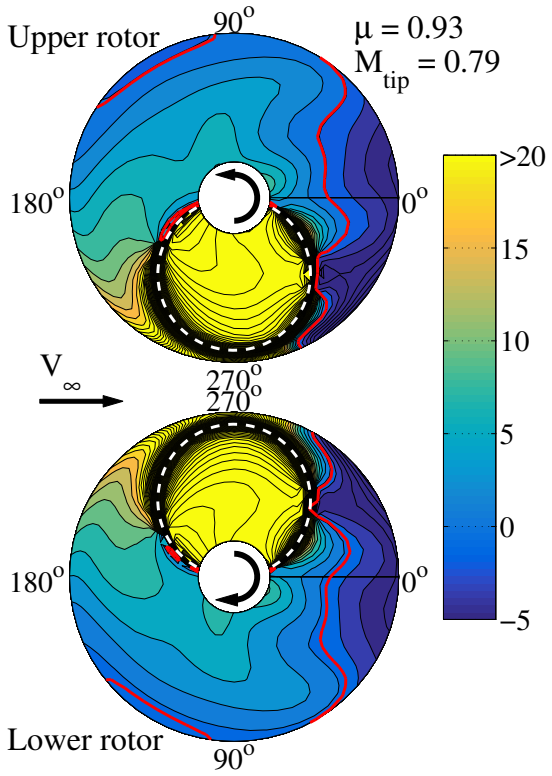

Fig. 28. Low vibration state, 70% nominal RPM $B_1' = -3°$: Angle of Attack, deg

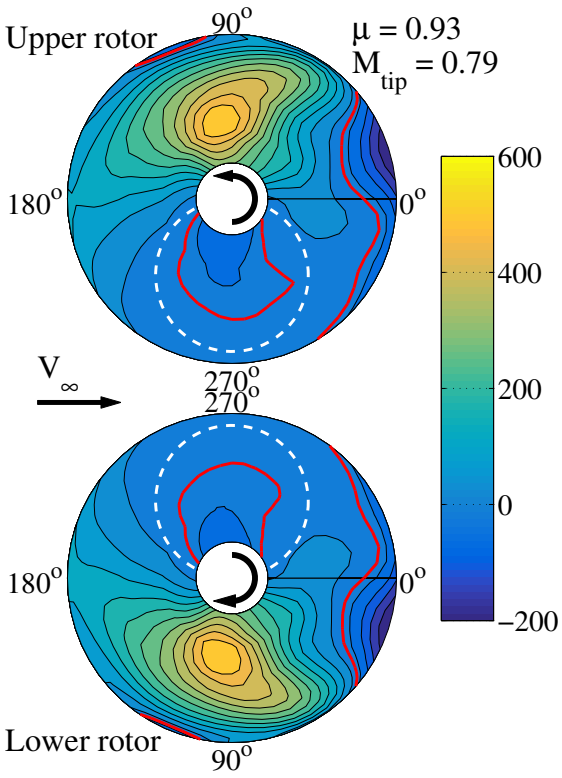

Fig. 29. Low vibration state, 70% nominal RPM B_1' = -3°: Blade lift, lbs/ft

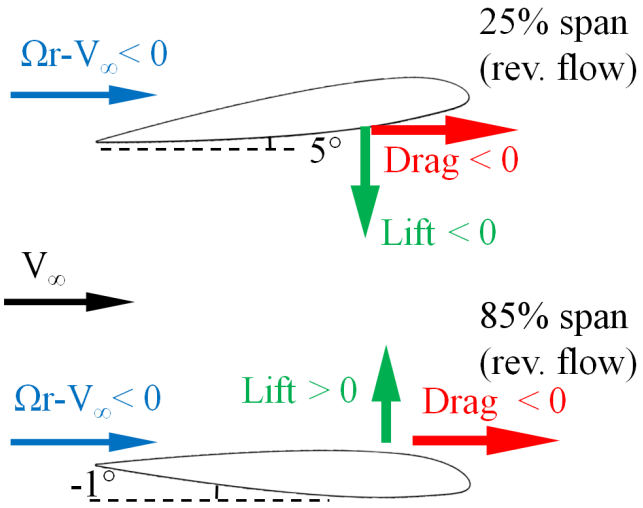

Fig. 30. Blade sections at 25% span (top) and 85% span (bottom) at ψ = 270°, low vibration state

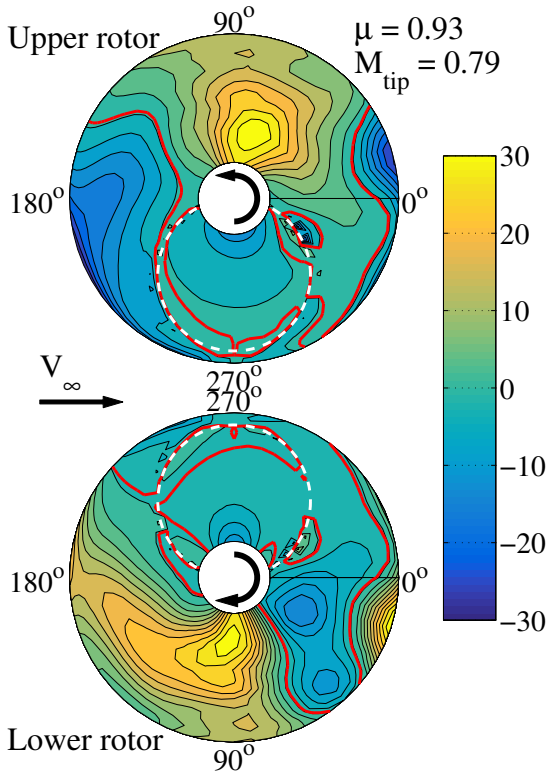

Fig. 31. Low vibration state, 70% nominal RPM B_1' = -3°: Blade drag, lbs/ft

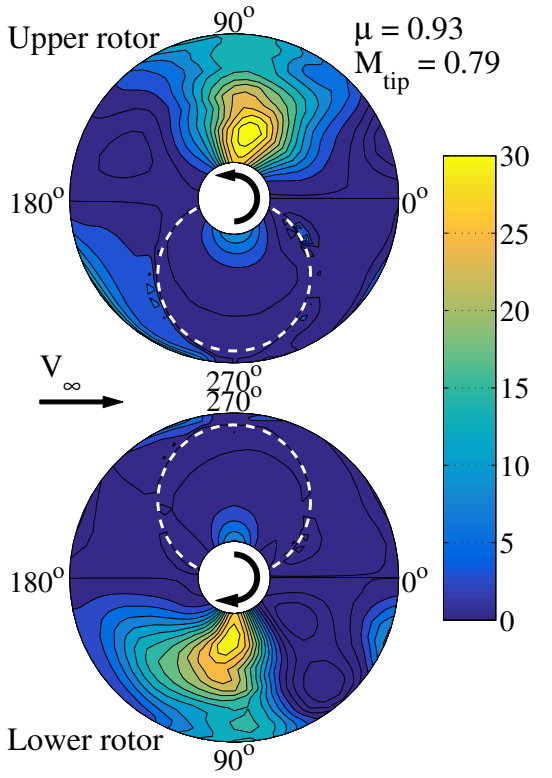

Fig. 32. Low vibration state, 70% nominal RPM B_1' = -3°: Blade H-force contribution, lbs/ft

Effect of differential lateral pitch

In the sections above it was observed that the low vibration state resulted in approximately 17% lower power requirement than the baseline at the expense of 31% increase in 3/rev vibratory forces while the 3/rev vibratory moments remained comparable. The differences between the low vibration state and the baseline state were a reduction in RPM from 97% to 70% nominal, and a change in differential lateral cyclic pitch from 2.5°to -3°. To answer the question as to whether the power reductions come predominantly from RPM reduction or change in differential lateral pitch, an additional operating point at 70% nominal RPM (same as the low vibration point), and 2.5 deg differential lateral (same as baseline) was considered.

Figure 33 shows the pitch variation, versus azimuth, for the 75% blade section at this new operating point. Also included, for comparison is the pitch variation for the low vibration point (previously shown on Fig. 22). Compared to the pitch variation for the baseline case on Fig. 22, the pitch variation for the new case at 70% nominal RPM and 2.5°differential lateral shows an increase in collective. The increase in pitch on the advancing side is necessary to generate the required lift with the reduced dynamic pressures associated with RPM reduction. The positive differential lateral cyclic adding to increased collective pitch, however, takes the pitch to very high values on the retreating side (seen in Fig. 33 to be about 13°higher than seen for the low vibration case)

Figures 34 and 35 show the rotor drag and H-force, respectively, for the 70% nominal RPM, 2.5 deg differential lateral case. In Fig. 34 the negative drag in the reverse flow region is seen to become very large near the root of the blade, compared to the low vibration case (Fig. 31) due to the very high angles of attack. Although this reduces main rotor power (from 94 hp for the low vibration case to 77 hp), it contributes very detrimentally to the rotor H-force (Fig. 35) which sees a large increase to 564 lbs (from 451 lbs for the low vibration case). While the contribution of the reverse flow region to rotor H-force was only 8.2% for the low vibration case, it increased to 38% for the 70% RPM, 2.5 deg differential lateral pitch case. This requires the propulsor force to increase from 3390 lbs for the low vibration case to 3475 lbs, resulting in a 93 hp increase in propulsive power. After accounting for the reduction in main rotor power, there is a net 76 hp increase in total power when differential lateral increases from -3 deg to +2.5 deg, while the rotor is operating at 70% nominal RPM.

While the low vibration case showed a 760 hp reduction in total power requirement, starting from the baseline operating state and reducing the RPM to 70% nominal (while holding the differential lateral pitch at 2.5 deg) itself reduces the power requirement by 683 hp. Starting from this point, holding at 70% nominal RPM, and reducing the differential lateral from 2.5°to -3°results in a relatively modest additional reduction of 77 hp. However, it should be noted from Fig. 14 that while moving from positive to negative values of differential lateral cyclic increases lift offset at higher RPM (over 80%), there a very small penalty in increased lift offset to be paid at below 70% RPM. Thus, the 77 hp reduction by changing from a positive to negative differential lateral pitch comes at little to no cost. From Figs 9 and 21, the 3/rev hub vibratory forces and moments too seem to be better at the low vibration state. In summary, it would appear that if the coaxial rotor RPM is to be reduced significantly to reduce power requirement, it is beneficial then to reverse differential lateral to get the required pitch on the advancing side while eschewing very high pitch on the retreating side. This appears to lead to additional reductions in power and vibration.

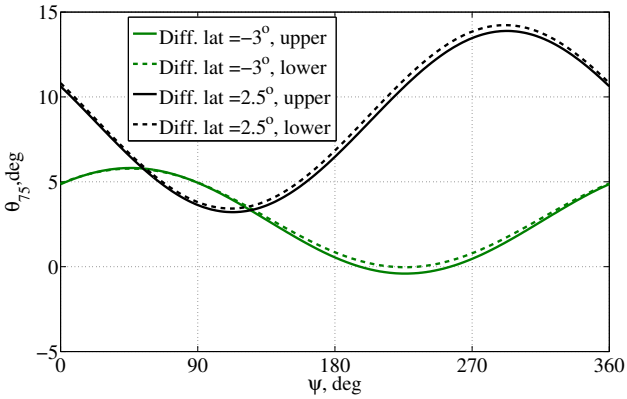

Fig. 33. Blade pitch at 70% of nominal RPM for two different values of differential lateral pitch

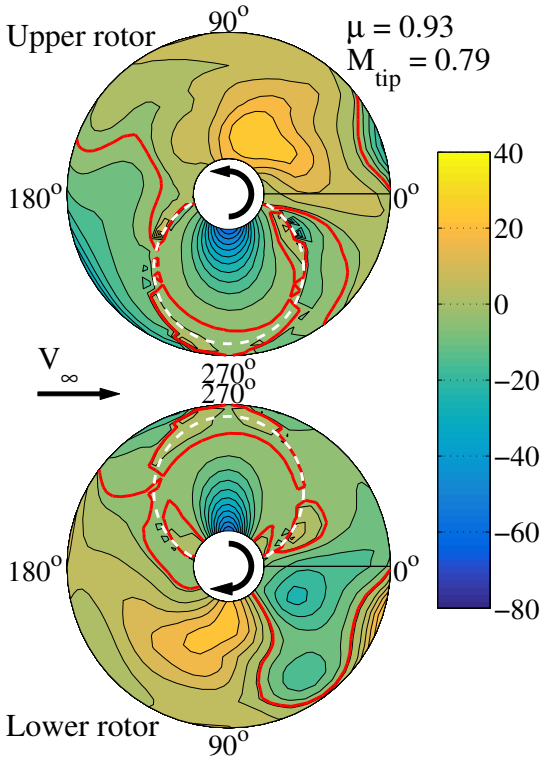

Fig. 34. 70% of nominal RPM, $B_1' = 2.5°$: Blade drag, lbs/ft

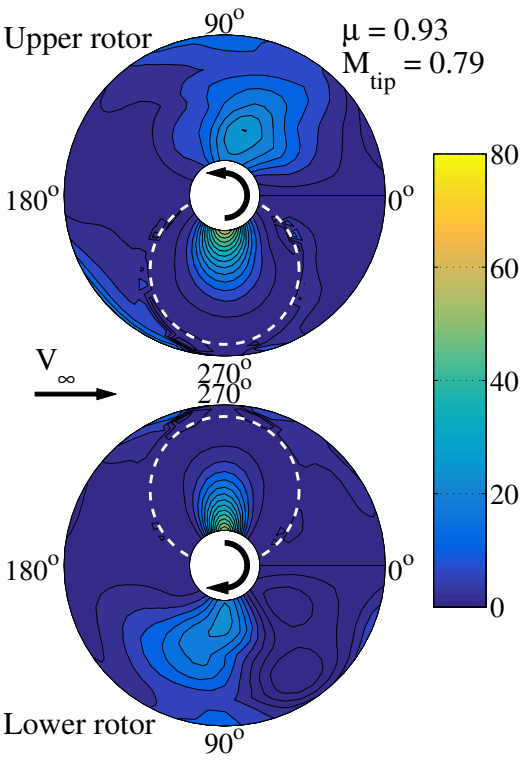

Fig. 35. 70% of nominal RPM, B_1' = 2.5°: Blade H-force contribution, lbs/ft

SUMMARY AND CONCLUSIONS

Optimal trim of the XH-59 aircraft in cruise flight at 250 kts was investigated using the RCAS comprehensive analysis. Low power and low vibration trim points were identified which corresponded to the minimum power condition and a condition which balanced low power and low 3/rev vibratory loads. Performance and loads of these trim points were analyzed in detail and compared to the baseline trim settings from flight test. From the calculations in this study, the following conclusions are offered:

1. The optimized trim settings reduced total power required by approximately 17%. This power reduction is obtained with a reduction in main rotor RPM from 97% nominal (for the baseline) to 70% nominal, and decrease in differential lateral pitch from 2.5°(for the baseline) to -3°.

2. At high speeds (250kts) fuselage and hub drag become increasingly large (3-4 times the rotor drag). In a compound coaxial helicopter, the propulsor power required to overcome the vehicle drag becomes the dominant contributor to total power, accounting for greater than 85% of the total power required.

3. Rotor slowing for this configuration was limited to 70% nominal because further reduction resulted in resonance of the first flap and chordwise modes and large vibratory loads.

4. The optimal state, producing about 17% power reduction, is accompanied by an increase in rotor lift offset to about 40%, which may be a constraint in practical design implementation.

5. Compared to the baseline, the 760 hp total reduction for the optimum operating condition came from a 520 hp reduction in main rotor power and a 240 hp reduction in propulsor power. The dominant contributors to reduction in main rotor power were the reduction in drag on the advancing blade tip due to reduction in advancing tip Mach number and negative angles of attack, as well as an increase in tip-path-plane blowback that put the rotor closer to an autorotative state. The reduction in drag on the advancing blade tip, as well as in the reverse flow region, reduced the rotor H-force by 230 lbs (from 851 to 621 lbs).

6. The -3°differential lateral pitch for the optimum case produces the required lift on the advancing side but keeps the angles of attack very low on the retreating side. The baseline case with +2.5°differential lateral results in higher angles of attack on the retreating side.

7. Reducing the rotor RPM alone down to 70% nominal while keeping the +2.5°differential lateral cyclic of the baseline produces a 683 hp reduction, with only an additional 77 hp reduction achieved by further reducing the differential lateral to -3°(while holding at 70% nominal RPM). However, this operating state results in very high blade pitch on the retreating side and a very large contribution (approaching 40%) of the reverse flow region to the total rotor H-force. Furthermore, the lift-offset is in the range of 40% (similar to the optimal point) and the vibration levels are greater. Thus, if rotor RPM is being reduced by 30% to minimize power, there appear to be multiple benefits without any obvious penalties, to reducing the differential lateral cyclic from positive to negative values.

Author contact: George Jacobellis, gjacobellis@gmail.com

REFERENCES

[1]Leishman, J. G., *The Helicopter - Thinking Forward, Looking Back*, College Park Press, College Park, MD, 2007.

[2]Ruddell, A., "Advancing Blade Concept (ABC) Technology Demonstrator," Technical report, U. S. Army Research and Technology Labotratories (AVRADCOM), USAVRADCOM-TR-81-D-5, Apr 1981.

[3]Felker, Fort F. III, "Performance and Loads Data from a Wind Tunnel Test of a Full-Scale, Coaxial, Hingless Rotor Helicopter," , October 1981.

[4]Phelps, A. E. and Mineck, R. E., "Aerodynamic Characteristics of a Counter-Rotating, Coaxial, Hingeless Rotor Helicopter Model With Auxiliary Propulsion," Technical report, National Aeronautics and Space Administration, NASA Technical Memorandum 78705, 1978.

[5]Ruddell, A. J., "XH-59A ABC Technology Demonstrator Altitude Expansion and Operational Tests," Technical Report USAAVRADCOM-TR-81-D-35, U. S. Army Research and Technology Laboratories (AVRADCOM), Dec 1981.

[6]Pleasants, W. A., "A Rotor Technology Assessment of the Advancing Blade Concept," Technical report, National Aeronautics and Space Administration, NASA Technical Memorandum 84298, 1983.

[7]O'Leary, J. and Miao, W., "Design of Higher Harmonic Control for The ABC," *Journal of the American Helicopter Society*, Vol. 27, (1), January 1982, pp. 52–57.

[8]Bagai, A., "Aerodynamic Design of the X2 Technology Demonstrator™ Main Rotor Blade," 64th Annual Forum of the American Helicopter Society, Montreal, Canada, April 2008.

[9]Blackwell, R. and Millot, T., "Dynamics Design Characteristics of the Sikorsky X2 Technology™ Demonstrator Aircraft," American Helicopter Society 64th Annual Forum, May 2008.

[10]Walsh, D., Weiner, S., Arifian, K., Bagai, A., Lawrence, T., and Blackwell, R., "Development Testing of the Sikorsky X2 Technology™ Demonstrator," 65th Annual Forum of the American Helicopter Society International, Grapevine,TX, 2009.

[11]Walsh, D., Wiener, S., Arifian, K., Lawrence, T., Wilson, M., Millott, T., and Blackwell, R., "High Airspeed Testing of the Sikorsky X2 Technology™ Demonstrator," 67th Annual Forum of the American Helicopter Society International, Virginia Beach, VA, 2011.

[12]Hirschberg, M., "Raider Rolls out," *Vertiflite*, Vol. 60, (6), Nov. 2014, pp. 12–13.

[13]Colucci, F., "No Single Decision," *Vertiflite*, Vol. 60, (6), Nov 2015, pp. 10–11.

[14]Syal, M. and Lieshman, J. G., "Aerodynamic Optimization Study of a Coaxial Rotor in Hovering flight," *Journal of the American Helicopter Society*, Vol. 57, (042003), 2012.
doi: 10.4050/JAHS.57.042003

[15]Lieshman, J. G. and Ananthan, S., "An Optimum Coaxial Rotor System for Axial Flight," *Journal of the American Helicopter Society*, Aug 2008, pp. 367–381.

[16]Rand, O. and Khromov, V., "Aerodynamic Optimization of Coaxial rotor in Hover and Axial Flight," 21st International Congress of the Aeronautial Sciences, 2010.

[17]Rand, O. and Khromov, V., "Compound Helicopter: Insight and Optimization," American Helicopter Society 69th Annual Forum, Phoenix, Arizona, May 2013.

[18]Hersey, S., Sridharan, A., and Celi, R., "Multiobjective Performance Optimization of a Coaxial Compound Rotorcraft Configuration," Fifth Decennial AHS Aeromechanics Specialists Conference, San Francisco, CA, Jan 2014.

[19]Giovanetti, E. B. and Hall, K. C., "Optimum Design of Compound Helicopters Using Higher Harmonic Control," AHS 70th Annual Forum, 2014.

[20]Yeo, H. and Johnson, W., "Investigation of Maximum Blade Loading Capability of Lift-Offset Rotors," *Journal of the American Helicopter Society*, Vol. 59, (012005), 2014.
doi: 10.4050/JAHS.59.012005

[21]Johnson, W., "Influence of Lift Offset on Rotorcraft Performance," AHS Specialist's Conference on Aeromechanics, San Francisco, CA, January 23-25, 2008.

[22]Floros, M. W. and Johnson, W., "Performance Analysis of the Slowed-Rotor Compound Helicopter Configuration," *Journal of the American Helicopter Society*, Vol. 54, (2), April 2009, pp. 1–12.
doi: 10.4050/JAHS.54.022002

[23]Floros, M. W. and Johnson, W., "Stability and Control Analysis of the Slowed-Rotor Compound Helicopter Configuration," *Journal of the American Helicopter Society*, Vol. 52, (3), Jul 2007, pp. 239– –253.
doi: 10.4050/JAHS.52.239

[24]Kim, H. W. and Brown, R. E., "Coaxial Rotor Performance and Wake Dynamics in Steady and Manoeuvering Flight," American Helicopter Society 62nd Annual Forum, 2006.

[25]Kim, H. W., Kenyon, A. R., Brown, R. E., and Duraisamy, K., "Interactional Aerodynamics and Acoustics of a Hingeless Coaxial Helicopter with an Auxiliary Propeller in Forward Flight," *The Aeronautical Journal*, Vol. 113, (1140), Feb 2009, pp. 65–78.

[26]Ferguson, K. and Thompson, D., "A Performance Analysis of Compound Helicopter Configurations," AHS 70th Annual Forum, Montreal, Canada, May 2014.

[27]Ferguson, K. and Thomson, D., "Flight Dynamics Investigation of Compound Helicopter Configurations," *Journal of Aircraft*, Vol. 52, 2015, pp. 156–167.
doi: 10.2514/1.C032657

[28]Sekula, M. K. and Gandhi, F., "Effects of Auxiliary Lift and Propulsion on Helicopter Vibration Reduction and Trim," *Journal of Aircraft*, Vol. 41, (3), May 2004, pp. 645–656.

[29]Sekula, M. K. and Gandhi, F., "Helicopter Vibration Reduction using Fixed-System Auxiliary Moments," *AIAA Journal*, Vol. 42, (3), March 2004, pp. 501 – 512.

[30]Sekula, M. K. and Gandhi, F., "Helicopter Vibration and Rotor Power Reduction through Horizontal Tail Incidence Angle Control," American Helicopter Society 60th Annual Forum, Baltimore, MD, June 2004.

[31]Gandhi, F. and Sekula, M. K., "Helicopter Horizontal Tail Incidence Control to Reduce Rotor Cyclic Pitch and Blade Flapping," American Helicopter Society 60th Annual Forum, Baltimore, MD, June 2004.

[32]Barron, H. M., Brentner, K., Hornand, J. F., Ozdemir, G., and Throsen, A., "Acoustic Analysis of Compound Helicopters with Trim Variations," American Helicopter Society 69th Annual Forum, Phoenix, AZ, May 2013.

[33]Reddinger, J.-P. and Gandhi, F., "A Physics-Based Approach to Trim Optimization of an Articulated Slowed-Rotor Compound Helicopter in High-Speed Flight," 70th American Helicopter Society Annual Forum, 2014.

[34]Saberi, H., Khoshlahjeh, M., Ormiston, R., and Rutkowski, M., "Overviewof RCAS and Application toAdvanced Rotorcraft Problems," AHS Fourth Decennial Specialists Conference on Aeromechanics, San Francisco, CA, Jan 2004.